Materials Letters 337 (2023) 133958

Contents lists available at ScienceDirect

Materials Letters

journal homepage: www.elsevier.com/locate/matlet

A dual-phase CrFeNbTiMo refractory high entropy alloy with excellent hardness and strength

Ba Chen [a], Xinmei Li [a,*], Yangyang Niu [b], Rui Yang [a], Wenjie Chen [a], Burebiye Yusupu [a], Liming Jia [a]

[a] School of Mechanical Engineering, Xinjiang University, Urumqi 830017, China
[b] State Key Laboratory of Nonlinear Mechanics, Institute of Mechanics, Chinese Academy of Sciences, Beijing 100190, China

ARTICLE INFO

Keywords:
Deformation and fracture
Intermetallic alloys and compounds
Phase diagrams

ABSTRACT

In order to the research of new type of coal mining machine cut-off tooth material, the CrFeNbTiMo high entropy alloy (RHEA) are studied and prepared. The microstructure is composed of BCC/B2 solid solution matrix phase and Laves phase. The alloy has a high strength of 785.26 MPa and a high hardness of 931 HV. In addition, the alloy also exhibits better ductility and strength under a split Hopkinson rod. The high strength and hardness of CrFeNbTiMo provides a new option for coal mining cut-off teeth.

1. Introduction

The refractory high entropy alloys have better high-temperature resistance [1], higher hardness [2] and strength [3]. Senkov et al.[4] developed two refractory high-entropy alloys: WTaNbMo and WTaNbMoV which have a single disordered BCC solid solution phase. It exhibits significantly superior mechanical properties at 1873 K, such as the yield strength of 477 MPa. But that contains Ta, W, and other elements with high price [5]. In this work, Cr, Fe, Nb, Ti and Mo are used to design a refractory high entropy alloy with high hardness and strength.

2. Material and methods

The metal blocks with a purity of more than 99.9 % were melted in a non-self-consuming vacuum arc furnace of type WK-II. The alloy ingot shall be turned over for smelting at least 7 times. The phase composition of the alloy was analyzed by a D&Advance X-ray diffractometer. The microstructure of the alloy was observed with a ZEISS SUPRA55 VP scanning electron microscope and EBSD (Electron Back Scatter Diffraction) detector. The hardness of the alloy was tested using an HXD-1000 TB microhardness tester, which was kept for 15 s at a load of 200 N. Ten points were measured, and the average value was calculated after removing the maximum and minimum values. The compression test by using ETM105D universal testing machine, the strain rate is $2\times10^{-4}/s^{-1}$. The sample size was ∅ 3 × 6 mm. The dynamic compression mechanical properties of the alloy at different strain rates were tested by using SHPB. The equilibrium phase diagram was constructed using Thermo-Calc (2020b) software and a TCHEA3 (high-entropy) database.

3. Results and discussion

The design of high-entropy alloys should not only consider the number of components but also their crystal structure [6]. After the research of many teams and scholars, mixture entropy (ΔSmix), mixture enthalpy (ΔHmix), atomic radius difference (δ), valence electron concentration (VEC) and parameter Ω are employed to predict the phase selection and phase stability in high-entropy alloys [7].

$$\Delta Smix = -\mathrm{R} \bullet \ln n \tag{1}$$

$$\Delta Hmix = \sum ni = 1i = j4\Delta H_{ij}^{mix} c_i c_j \tag{2}$$

$$\boldsymbol{\delta} = \sqrt{\sum_{i=1}^{n} \boldsymbol{c_i}(1 - r_i/\bar{r})^2}; \bar{\boldsymbol{r}} = \sum_{i=1}^{n} c_i r_i \tag{3}$$

$$VEC = \sum_{i=1}^{n} c_i (VEC)_i \tag{4}$$

$$\Omega = \boldsymbol{T_m}\Delta\boldsymbol{S_{mix}}/|\Delta\boldsymbol{H_{mix}}|; \boldsymbol{T_m} = \sum_{i=1}^{n} c_i (T_m)_i \tag{5}$$

* Corresponding author.
E-mail address: lxmxj2009@126.com (X. Li).

https://doi.org/10.1016/j.matlet.2023.133958
Received 8 December 2022; Received in revised form 18 January 2023; Accepted 21 January 2023
Available online 25 January 2023

where R is gas constant, ci and cj are the mole fractions of constituents i and j, ΔHij is the enthalpy of mixture between constituent i and j, ri is the atomic radius of constituent i, $\bar{r}$ is the average radius of the elements contained.

The calculated empirical parameters and predicted phases are shown in Fig. 1. The values of the various parameters of the CrFeNbTiMo are within the numerical range of forming a disordered solid solution phase. That indicating the disordered solid solution phase composition of the alloy has high structural stability. Shown in the Fig. 1 is the enthalpy of binary mixing of the alloy. The FeTi intermetallic compounds have a B2-type that spatial group is Pm3m (221); $FeTi_2$ is *P63/mmc* (194). The $NbFe_2$ belongs to the C15-Laves and the spatial group is Fd3m. The $NbCr_2$ is characterized by C15-Laves structure at low temperature, C14-Laves and C36-Laves structure that is transitional and has a low probability of occurrence at high temperature, are formed between Cr and Nb elements. The $TiCr_2$ is C15-Laves with the space group Fd3m (227) [8].

Fig. 2(a) shows a pseudo-binary phase diagram of the equilibrium state of the alloy calculated by using the thermodynamic software Thermo-Calc. The alloy showing the melting point of alloying elements is about 2500 °C. In addition, the alloy solidifies in the temperature range of 1600 °C-1870 °C, BCC/B2 solid solution and C14-Laves phase is formed after solidification. Studies by many scholars show that the Nb element will promote the precipitation of the Laves phase inside the alloy, which is a typical topological dense row (TCP) phase with room temperature brittleness and low fracture toughness.

Fig. 2(b) shows the non-equilibrium solidification phase diagram of the CrFeNbTiMo calculated using the Scheil-Gulliver model. Between T_1 = 794.7 °C and T_3 = 1029.7 °C the alloy will solidification. The alloy will first form the BCC/B2 phase at 1794.7 °C and the C14-Laves phase begins to form when the temperature was reduced to 1509.4 °C. Finally, the alloy is completely solidified at 1029.7 °C and a trace amount of $NiTi_2$ compounds will precipitate at this point. The $NiTi_2$ compound does not appear in the phase composition because of the special high entropy effect of high entropy alloy thermodynamics.

Fig. 3(d) is the XRD pattern of CrFeNbTiMo RHEAs. It can be seen the RHEA is a biphasic structure with the simple body-centered cube (BCC/B2) and intermetallic compound (Laves). The B2 phase of the alloy is determined based on the comparison with the PDF card and the small peak that appears at about 30.7° in the XRD diagram [9]. The diffraction peak of the Laves phase can be observed, the second phase structure produced by the alloy may be the Laves phase structure.

BSE images of the RHEA sample are shown in Fig. 3(e). The alloy is a typical branch crystal morphology showing a clear contrast of the tissue. It can be seen that the branch crystal (BCC/B2) enriches the Mo element; the inter-dendrite (Laves) enriches the Cr and Fe elements; the Nb and Ti elements are relatively uniformly distributed in the alloy. It shows that the alloy undergoes obvious segregation when solidifying, it is mainly closely related to the melting point of the alloy and its interaction. The Mo elements have a relatively higher melting point in the process of smelting and solidification of alloys. They will solidify and form branch crystal structures preferentially, while Cr and Fe elements do not grow up too long and are segregated to the inter-dendrite region because of the lower melting points. It can be inferred that the alloy dendrite and inter-dendrite structure may be BCC/B2 and Laves phase structure. The Laves phase be $FeTi_2$ and $NbCr_2$ structures combined with EDS and XRD. At the same time, the difference in the atomic radius of alloying elements has an important impact on the formation of solid solutions and intermetallic compounds. The difference in atomic size leads to the prominent lattice constant of the BCC solid solution and produces a significant lattice distortion effect.

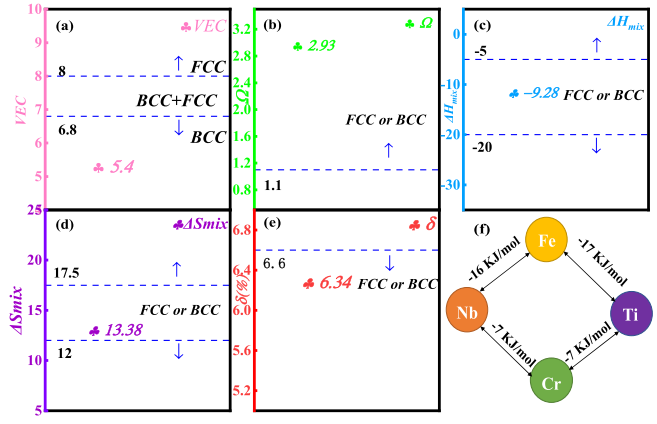

Fig. 1. VEC, Ω, ΔH_{mix}, ΔS_{mix},δ and Binary mixing enthalpy of the CrFeNbTiMo RHEAs.

Fig. 3(b) is a phase diagram of the CrFeNbTiMo RHEAs obtained by EBSD technology. In the EBSD pattern, the B2 phase was not detected. It can be speculated that the B2 phase of the alloy is likely to the form of nanoscale particles distributed in the BCC matrix. Fig. 3(c) shows the grain size distribution of the alloy, and the average grain size of the alloy is calculated to be 3.477 μm. Fig. 3(a) is the inverse pole figure of the EBSD. From which it can be observed that the vast majority of the analyzed area has a crystallographic texture close to the direction of [101].

Fig. 4 (a) shows the room temperature compression performance of the alloy. The compressive strength of the alloy is 785.26 MPa and the fracture strain is 5.43 %.The hardness is 931 HV. It can be seen that the CrFeNbTiMo RHEAs have a high hardness and high strength. But the alloy is less plastic. The XRD map of CrFeNbTiMo RHEAs shows that the alloy has a second phase Laves phase precipitation. The main strengthening mechanism in the alloy is solid solution strengthening and precipitation phase strengthening. Which increases the difficulty of dislocation nucleation and slips and results in an increase in its strength. But the brittle behavior of the Laves phase leads to low ductility of the alloy at room temperature. At the same time, the Laves-type precipitation phase produced by the alloy also produces a diffusion-strengthening effect and improves the hardness and strength of the alloy to a certain extent. The high hardness and high strength of the alloy are derived from the solid solution strengthening effect of the BCC phase and the precipitation strengthening effect of the second hard phase Laves phase. The precipitation strengthening is another strengthening mechanism of the alloy. However, the precipitation phase also has an impact on the toughness of the alloy.

Fig. 4(b and c) shows the stress–strain curve and fracture morphology of the alloy at the strain rate of 1945.7 s^{-1} and 2652 s^{-1}. As shown in Fig. 4(b and c), the compressive strength and fracture strain under the dynamic of the material are significantly improved compared with the static. The alloy is completely fractured under the two strain rates used in the experiment, showing a clear yield process and the stress curve is instantaneously. Oscillations on curves 4 (b,c) can be associated with the formation of delaminations or the merging of groups of micropores. When it reaches the highest point ('stress collapse' phenomenon), which indicated the plasticity of the alloy is poor.

It is visible that there are obvious river-like patterns on the fault surface from the fracture morphology of the alloy in Fig. 4(d–g). There are macroscopic fault steps of different heights and a large number of river-like and tongue-like patterns in Fig. 4(d–g). These characteristics indicate RHEA under brittle fracture under dynamic strain load and the cleavage fracture mechanism is presented at break time [10].

4. Conclusions

In this study, the CrFeNbTiMo alloy with the BCC/B2 phase of Mo-rich elements and the Laves phase of Cr-rich and Fe-rich elements. The CrFeNbTiMo alloy hardness is as high as 931HV. The fracture strength is 785.26 MPa and the fracture strain is 5.43 %. The CrFeNbTiMo alloy has a strength of 1630 MPa and 1050 MPa under dynamic loads of 1945.7 s^{-1} and 2652 s^{-1}. The morphology of the fracture shows

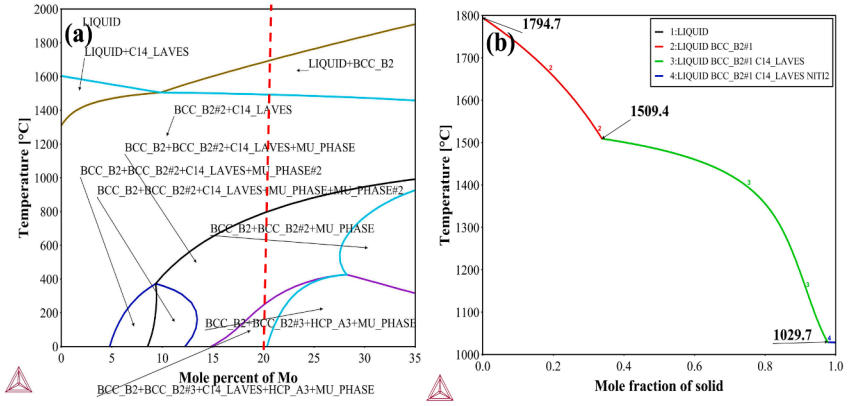

Fig. 2. Equilibrium phases and non-equilibrium solidification phase in the CrFeNbTiMo RHEA.

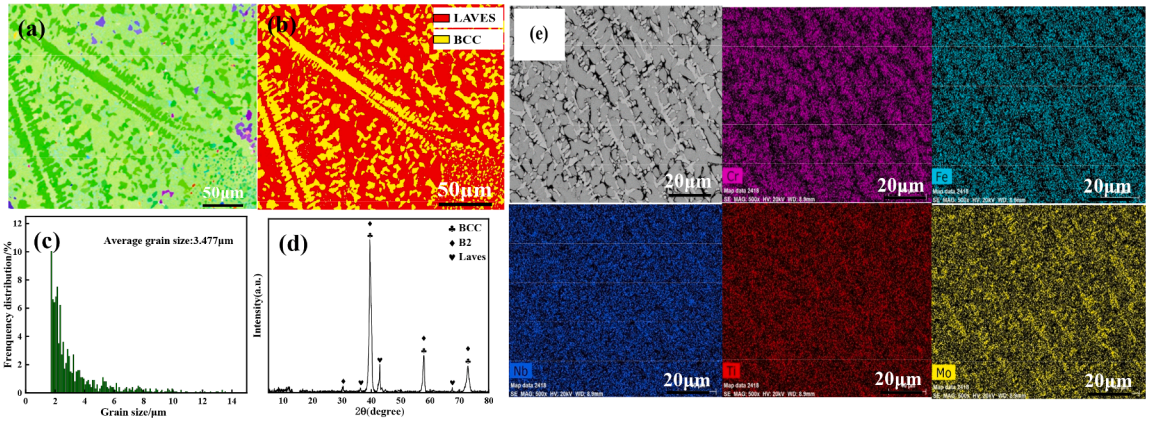

Fig. 3. (a) EBSD inverse pole figure; (b) phase figures;(c) grain size; (d) XRD pattern and (e) SEM-BSE mapping of CrFeNbTiMo RHEAs.

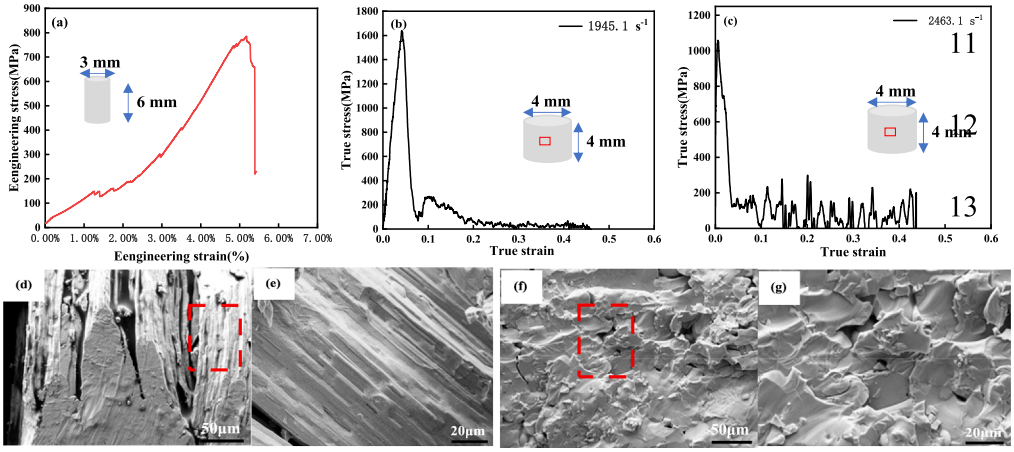

Fig. 4. True stress–strain curves under dynamic compression (b, d) and Electron microscopy (c, e) of CrFeNbTiMo RHEAs.

obvious river-like patterns and fault steps, manifested as a brittle fault.

CRediT authorship contribution statement

Ba Chen: Methodology, Data curation, Writing – review & editing, Investigation. **Xinmei Li:** Funding acquisition, Project administration, Investigation, Supervision. **Yangyang Niu:** Formal analysis, Investigation, Validation. **Rui Yang:** Data curation, Investigation. **Wenjie Chen:** Investigation. **Burebiye Yusupu:** Validation. **Liming Jia:** Data curation.

Declaration of Competing Interest

The authors declare that they have no known competing financial interests or personal relationships that could have appeared to influence the work reported in this paper.

Data availability

Data will be made available on request.

Acknowledgements

The work was supported by National Natural Science Foundation of China (No. 52161017, 51865055) and Natural Science Foundation of Xinjiang Uygur Autonomous Region (2022D01C386). We also thank the software support from University of Science and Technology Beijing.

References

[1] D.B. Miracle, O.N. Senkov, Acta Mater. 122 (2017) 448–511.
[2] E.P. George, D. Raabe, R.O. Ritchie, Nat. Rev. Mater. 4 (2019) 515–534.
[3] Y. Han, H.B. Li, H. Feng, Y.Z. Tian, Z.H. Jiang, T. He, Mater. Sci. Eng. A 814 (2021).
[4] O.N. Senkov, S.V. Senkova, C.F. Woodward, Acta Mater. 68 (2014) 214–228.
[5] S.G. Ma, Z.M. Jiao, J.W. Qiao, H.J. Yang, Y. Zhang, Z.H. Wang, Sci. Eng. A 649 (2016) 35–38.
[6] S. Huang, H. Wu, H.G. Zhu, Z.H. Xie, Mater. Sci. Eng. A 809 (2021).
[7] Y.Z. Shi, Y. Bin, X. Xie, J. Brechtl, K.A. Dahmen, P.K. Liaw, Corros. Sci. 119 (2017) 33–45.
[8] X.J. Fan, R.T. Qu, Z.F. Zhang, J. Mater. Sci. 123 (2022) 70–77.
[9] R.J. Scales, D.E.J. Armstrong, A.J. Wilkinson, B.S. LI, Materialia. 4 (2020):100940.
[10] I. Konovalenko, P. Maruschak, J. Brezinová, J. Brezina, Mater. 12 (2019) 2051.